PAPER

Spectral tunability of two-photon states generated by spontaneous four-wave mixing: fibre tapering, temperature variation and longitudinal stress

Quantum Science and Technology

RECEIVED
16 March 2017

REVISED
26 May 2017

ACCEPTED FOR PUBLICATION
19 June 2017

PUBLISHED
2 August 2017

PAPER

Spectral tunability of two-photon states generated by spontaneous four-wave mixing: fibre tapering, temperature variation and longitudinal stress

E Ortiz-Ricardo[1], C Bertoni-Ocampo[1], Z Ibarra-Borja[2], R Ramirez-Alarcon[2], D Cruz-Delgado[1], H Cruz-Ramirez[1], K Garay-Palmett[3] and A B U'Ren[1]

[1] Instituto de Ciencias Nucleares, Universidad Nacional Autónoma de México, Apartado Postal 70-543, 04510 DF, México
[2] Centro de Investigaciones en Optica A.C., Loma del Bosque 115, Colonia Lomas del Campestre, 37150 León Guanajuato, México
[3] Departamento de Óptica, Centro de Investigación Científica y de Educación Superior de Ensenada, Apartado Postal 360 Ensenada, BC 22860, México

E-mail: kgaray@cicese.mx

Keywords: spontaneous four-wave mixing, quantum entanglement, optical fibres

Abstract

We explore three different mechanisms designed to controllably tune the joint spectrum of photon pairs produced by the spontaneous four-wave mixing (SFWM) process in optical fibres. The first of these is fibre tapering, which exploits the modified optical dispersion resulting from reducing the core radius. We have presented a theory of SFWM for tapered fibres, as well as experimental results for the SFWM coincidence spectra as a function of the reduction in core radius due to tapering. The other two techniques that we have explored are temperature variation and application of longitudinal stress. While the maximum spectral shift observed with these two techniques is smaller than for fibre tapering, they are considerably simpler to implement and have the important advantage that they are based on the use of a single, suitably controlled, fibre specimen.

1. Introduction

During the past few decades, photon pairs generated through spontaneous parametric processes have served as the basis for many important advances in quantum-enhanced technologies such as quantum metrology [1], quantum communications [2] and quantum computation [3]. In particular, the process of spontaneous four-wave mixing (SFWM) implemented in fibres or waveguides has gained prominence as an alternative to spontaneous parametric downconversion (SPDC) based on second-order nonlinear crystals [4–7].

The properties of photon pairs generated by SFWM depend on the optical dispersion experienced by the four participating waves [8]. Thus, the use of specialty fibres, for example including photonic crystal [9], highly nonlinear [10], multi-cladding [11] and chalcogenide [12] fibres may be exploited for the generation of two-photon states with engineered properties at particular spectral ranges. However, an approach based on the design of specific fibre structures is both expensive and possibly impractical. Among the categories of two-photon state engineering, perhaps the simplest is controllable spectral tuning of a particular quantum state, while otherwise maintaining the structure of the two-photon state. Such spectral tuning can be a practical necessity so as to attain mode matching with other optical fields, so as to attain emission at the highest detection efficiencies of single-photon detectors, or if the photon pairs are sufficiently narrowband so as to match photon pairs with particular electronic transitions in atoms or quantum dots. Furthermore, it would be highly desirable if such tuning could be accomplished in the laboratory by variation of an appropriate physical parameter of a *single* source specimen, without the need for drawing from a collection of fibres designed with different properties so as to achieve the spectral tuning.

In this paper, we set out to explore three different mechanisms for spectrally tuning the two-photon state produced by the spontaneous four-wave mixing (SFWM) process in birefringent optical fibres. These three

mechanisms are (i) fibre tapering, (ii) fibre heating and (iii) the application of longitudinal stress. In section 2 we present the relevant theory which may be used to predict the SFWM two-photon state generated in a tapered fibre, which can also be used in the appropriate special cases to predict the two-photon state obtained for a heated and/or longitudinally stressed untapered fibre. Although we specialise our theory for fibre-taper devices of the sort that we can fabricate in our laboratory, the framework developed can be used to predict the two-photon state for fibres with a more general longitudinally varying radius profile [13], which could be useful in other situations.

Note that fibre tapers have been proposed [14] and used previously in the context of nonlinear optics for supercontinuum generation [15], third-harmonic generation [16] and for photon-pair generation based on the SFWM process [17]. In this paper we show that the use of fibre tapers for photon-pair emission through SFWM with controllable spectral properties is a practical proposition. However, we also show that the application of temperature variation and/or application of longitudinal stress to the SFWM fibre constitute simpler alternatives for photon-pair spectral tuning, and can be based on a suitably controlled single fibre.

2. Theory of spontaneous four-wave mixing in tapered fibres

The process of spontaneous four-wave mixing in third-order nonlinear media, such as optical fibres, involves the annihilation of two pump photons (with frequencies ω_1 and ω_2, respectively), and the simultaneous emission of a photon pair, comprised of a photon with frequency ω_s (signal) and a photon with frequency ω_i (idler), under the fulfilment of energy and momentum conservation [4, 8].

In a single-mode optical fibre of length L, assuming that the four participating waves are co-polarised and travel along the fibre in the same direction (z-axis), the SFWM process produces the state $|\Psi\rangle = |0\rangle + \eta|\Psi_2\rangle$ [18], where η is a constant related to conversion efficiency and the two-photon contribution $|\Psi_2\rangle$ is given by

$$|\Psi_2\rangle = \int d\omega_s \int d\omega_i \, G(\omega_s, \omega_i)\hat{a}^\dagger(\omega_s)\hat{a}^\dagger(\omega_i)|0\rangle_s|0\rangle_i, \tag{1}$$

in terms of the joint spectral amplitude (JSA) function $G(\omega_s, \omega_i)$, which is obtained by the coherent addition of the contributions from all successive segments of the fibre as

$$G(\omega_s, \omega_i) = \int_0^L dz J(z)\ell(\omega_s, z)\ell(\omega_i, z)f(\omega_s, \omega_i, z) \tag{2}$$

in terms of the creation operator $\hat{a}^\dagger(\omega_\mu)$ for the signal ($\mu = s$) and idler ($\mu = i$) modes. A defining aspect of a tapered fibre is that the core radius and hence the fibre characteristics including the pump/SFWM indices of refraction and wavenumbers, are dependent on the position z along the fibre. Therefore, in the above equation, the functions $J(z)$, $\ell(\omega_\mu, z)$ and $f(\omega_s, \omega_i, z)$ are z-dependent. The function $J(z)$ is given as follows:

$$J(z) = \frac{F_{eff}(z)}{n(\omega_{p0}, z)}, \tag{3}$$

where $n(\omega_{p0}, z)$ is the effective refractive index of the propagating fibre mode evaluated at the pump central frequency, and $F_{eff}(z)$ is the spatial overlap integral between the four fields expressed as

$$F_{eff}(z) = \int dx \int dy f_1(x, y, z)f_2(x, y, z)f_s^*(x, y, z)f_i^*(x, y, z), \tag{4}$$

with $f_m(x, y, z)$ ($m = 1, 2, s, i$) the transverse spatial field distribution at the longitudinal position z, which is normalised so that $\int dx \int dy |f_m(x, y, z)|^2 = 1$ and is approximated to be frequency-independent within the pump and SFWM emission bandwidths.

The function $\ell(\omega_\mu, z)$ is given as follows:

$$\ell(\omega_\mu, z) = \left[\frac{\hbar\omega_\mu k'^2(\omega_\mu, z)}{\pi\epsilon_0 n^2(\omega_\mu, z)}\right]^{\frac{1}{2}}, \tag{5}$$

where $\hbar$ is Planck's constant, ϵ_0 the vacuum electric permittivity, $n(\omega_\mu, z)$ the effective refractive index of the mode propagating along the fibre and $k'(\omega_\mu, z)$ the first derivative of the propagation constant.

The function $f(\omega_s, \omega_i, z)$ is given as follows:

$$f(\omega_s, \omega_i, z) = \int d\omega \alpha(\omega)\alpha(\omega_s + \omega_i - \omega)e^{i\Delta k(z)z}, \tag{6}$$

given in terms of the pump spectral envelope $\alpha(\omega)$ and the phasemismatch $\Delta k(z)$ defined as

$$\Delta k(z) = k(\omega, z) + k(\omega_s + \omega_i - \omega, z) - k_s(\omega_s, z) - k_i(\omega_i, z) - \phi_{NL}, \tag{7}$$

where ϕ_{NL} is a nonlinear phase shift derived from self/cross-phase modulation [19]. Note that the treatment presented here focuses on the degenerate pumps case, i.e. the two pump photons come from the same field, which is assumed to have a Gaussian spectral envelope centred at ω_{p0} and with a bandwidth σ.

In this section of the paper, we analyse the SFWM two-photon state produced by an optical fibre taper, with a radius profile along the z-axis composed of five zones as sketched in figure 1: (i) an unstretched zone of radius r_0 and length L_c, (ii) a transition zone, of length z_0, along which the radius diminishes with increasing z down to a value r_w, (iii) a waist zone of length L_w characterised by a constant radius r_w, (iv) a second transition zone, also of length z_0, along which the radius increases with increasing z up to the unstretched radius r_0, and (v) a second unstretched zone, also of length L_c, of radius r_0. It is assumed that the two transition zones are adiabatic, with an exponential dependence of the radius with z; the specific taper radius profiles can be predicted through volume conservation; see Birks et al [20].

Our approach is to subdivide the fibre in the two transition zones into N sections of length δL (see figure 1) which are assumed to be short enough that the integral in equation (2) over such a fibre interval may be approximated by the integrand evaluated at intermediate radius $\bar{r}_m = (r_m + r_{m-1})/2$ with $m = 1, 2, 3 ..., N$, multiplied by δL. In this case, the integral in equation (6) may be expressed in terms of the contributions from the five sections introduced in the previous paragraph as follows:

$$\begin{aligned}\int_0^L dz\, e^{i\Delta k(z)z} = \int_0^{L_c} dz\, e^{i\Delta k^{\downarrow}_{r_0} z} + \delta L \sum_{m=1}^{N} e^{i\Delta k^{\downarrow}_{\bar{r}_m}[L_c+(m-1/2)\delta L]} + \int_{L_c+z_0}^{L_c+z_0+L_w} dz\, e^{i\Delta k_{r_w} z} \\ + \delta L \sum_{m=1}^{N} e^{i\Delta k^{\uparrow}_{\bar{r}_m}[L_c+z_0+L_w+(m-1/2)\delta L]} + \int_{L_c+2z_0+L_w}^{2L_c+2z_0+L_w} dz\, e^{i\Delta k^{\uparrow}_{r_0} z},\end{aligned} \tag{8}$$

where the downward arrow designates the first unstretched zone and first transition zones and the upward arrow designates the second transition zone and the second unstretched zone. This integral is given in terms of radius-dependent phasemismatch terms $\Delta k_r^{\downarrow}$ (for zones 1 and 2), Δk_r (for the waist, or zone 3), and $\Delta k_r^{\uparrow}$ (for zones 4 and 5).

The two-photon joint spectral amplitude $G(\omega_s, \omega_i)$ for the entire fibre taper composed of the five subsequent segments may then be expressed as

$$G(\omega_s, \omega_i) = F^{\downarrow}_{r_0}(\omega_s, \omega_i) + F^{\downarrow}_{z_0}(\omega_s, \omega_i) + F_{r_w}(\omega_s, \omega_i) + F^{\uparrow}_{z_0}(\omega_s, \omega_i) + F^{\uparrow}_{r_0}(\omega_s, \omega_i), \tag{9}$$

where the contributions from the five zones are expressed as follows:

$$F^{\downarrow}_{r_0}(\omega_s, \omega_i) = \eta_{r_0}(\omega_s, \omega_i) \int d\omega \alpha(\omega)\alpha(\omega_s + \omega_i - \omega)\,\mathrm{sinc}\left[\frac{L_c \Delta k^{\downarrow}_{r_0}}{2}\right] e^{i\frac{L_c}{2}\Delta k^{\downarrow}_{r_0}}, \tag{10}$$

$$F^{\downarrow}_{z_0}(\omega_s, \omega_i) = \delta L \int d\omega \alpha(\omega)\alpha(\omega_s + \omega_i - \omega) \times \sum_{m=1}^{N} \eta_{r_m}(\omega_s, \omega_i) e^{i\Delta k^{\downarrow}_{\bar{r}_m}[L_c+(m-1/2)\delta L]}, \tag{11}$$

$$F_{r_w}(\omega_s, \omega_i) = \eta_{r_w}(\omega_s, \omega_i) \int d\omega \alpha(\omega)\alpha(\omega_s + \omega_i - \omega)\,\mathrm{sinc}\left[\frac{L_\omega \Delta k_{r_w}}{2}\right] \times e^{i\frac{L_w}{2}\Delta k_{r_w}} e^{i[L_c+z_0]\Delta K_{r_w}}, \tag{12}$$

$$F^{\uparrow}_{z_0}(\omega_s, \omega_i) = \delta L \int d\omega \alpha(\omega)\alpha(\omega_s + \omega_i - \omega) \times \sum_{m=1}^{N} \eta_{r_m}(\omega_s, \omega_i) e^{i\Delta k^{\uparrow}_{\bar{r}_m}[L_c+z_0+L_w+(m-1/2)\delta L]}, \tag{13}$$

$$F^{\uparrow}_{r_0}(\omega_s, \omega_i) = \eta_{r_0}(\omega_s, \omega_i) \int d\omega \alpha(\omega)\alpha(\omega_s + \omega_i - \omega)\,\mathrm{sinc}\left[\frac{L_c \Delta k^{\uparrow}_{r_0}}{2}\right] \times e^{i\frac{L_c}{2}\Delta k^{\uparrow}_{r_0}} e^{i[L_c+L_w+2z_0]\Delta K^{\uparrow}_{r_0}}. \tag{14}$$

In equations (10)–(14), the phasemismatch term Δk_{r_μ} is given according to equation (7). We have introduced the parameter η_{r_μ} (with r_μ the local core radius), which is given by

$$\eta_{r_\mu}(\omega_s, \omega_i) = J(r_\mu)\ell(\omega_s, r_\mu)\ell(\omega_i, r_\mu), \tag{15}$$

with $J(.)$ and $\ell(.)$ defined in equations (3) and (5), respectively, for the corresponding r_μ.

From the JSA function $G(\omega_s, \omega_i)$, one may obtain the joint spectral intensity $|G(\omega_s, \omega_i)|^2$ which corresponds to the two-dimensional probability distribution of generating a photon pair with frequencies ω_s and ω_i. In our experiments reported later in this paper, we have measured coincidence spectra which are the result of spectrally-resolving one photon of each pair, say the signal photon, and detecting it in coincidence with the conjugate (non spectrally resolved) idler photon. The resulting spectra can be evaluated from the joint spectral intensity as

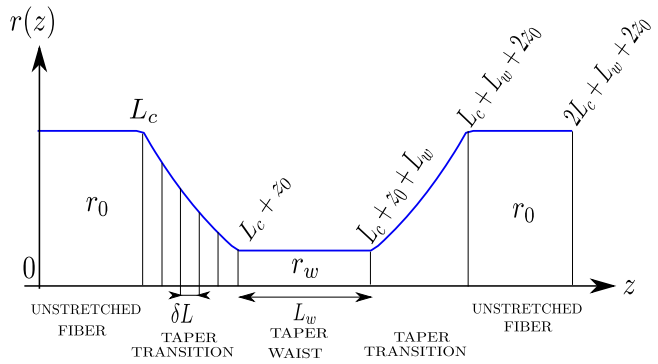

Figure 1. Fibre-taper profile used for SFWM photon-pair generation.

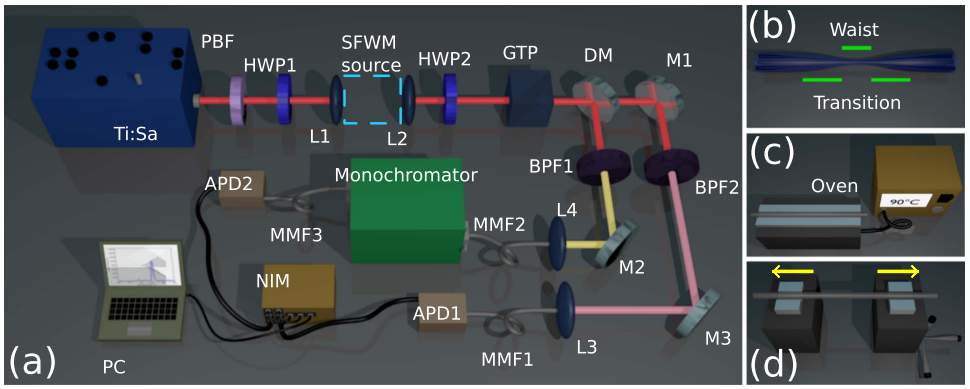

Figure 2. (a) Experimental setup designed to measure coincidence spectra; all the elements in the setup are explained in section 3.1. The SFWM source (fibre taper, heated fibre or longitudinally stressed fibre) is situated within the dotted box between lenses L1 and L2. The three types of source are sketched in panels (b)–(d): (b) fibre taper, (c) heated fibre and (d) longitudinally stressed fibre.

$$f_s(\omega_s) = \int d\omega_i |G(\omega_s, \omega_i)|^2. \tag{16}$$

As will become apparent below, the structure of coincidence spectra generated in a tapered fibre, depends significantly on the relative lengths of the five zones along the taper. Note that for a fibre with a constant core radius, the JSA would be given by equation (10) by replacing L_c with the corresponding fibre length.

3. Experimental implementation of SFWM in a bow-tie fibre

3.1. Experimental setup

We have implemented a SFWM photon-pair source based on a polarisation maintaining optical fibre, specifically a bow-tie fibre (model HB800C), from Fibercore Ltd. In this type of fibre, as we have shown before, SFWM can be phasematched according to a cross-polarised scheme in which the pump photons are polarised parallel to the fibre slow axis, while the SFWM photons are polarised parallel to the fibre fast axis; we determined from SFWM measurements the parameters for this fibre: core radius $r = 1.45$ μm, numerical aperture $NA = 0.20$ and birefringence $\Delta = 2.38 \times 10^{-4}$ [21, 22]. Note that while in our previous work [22] we produced inter-modal SFWM, i.e. with contributions from different combinations of transverse modes for four participating waves, in this paper we focus on the SFWM process involving all four waves (degenerate pumps, signal, and idler) propagating in the fundamental mode.

The setup used for our two-photon spectral tuning experiments is depicted in figure 2(a). This setup is designed to measure the coincidence spectra for different source configurations involving the use of the SFWM fibre: (i) tapered with a varying waist radii (see figure 2(b)), (ii) heated to a varying temperature (see figure 2(c)) or (iii) longitudinally stressed to a varying degree (see figure 2(d)).

We have used as a pump a picosecond mode-locked Ti:sapphire laser centred at 715 nm with a ~0.5 nm bandwidth, and 76 MHz repetition rate. The pump spectrum is filtered with a prism-based spectral bandpass filter (PBF), and its polarisation is set parallel to the fibre's slow axis with the use of a half wave plate (HWP1). We

Table 1. Parameters of the fabricated fibre tapers. The core radius of the untapered fibre is $r_0 = 1.45$ μm. All tapers have a waist length $L_w = 2.5$ cm. % indicates the percentage of diameter reduction at the waist with respect to the unstretched fibre.

%	$r_w(\mu m)$	z_0(cm)	L_c(cm)	L(cm)
70	1.01	0.89	10.36	25
75	1.09	0.72	9.53	23
80	1.16	0.56	8.69	21
85	1.23	0.41	9.84	23
90	1.30	0.26	8.54	20.1
95	1.38	0.13	7.42	17.6
100	1.45			11.3

couple the pump into the fibre using an aspheric lens with 8 mm focal length (L1). We use a 3-axis flexure stage (Thorlabs MAX350D) for coupling the pump into the fibre. The photon pairs are outcoupled from the fibre (the outcoupled power ranges from ∼40 mW to ∼70 mW) using another aspheric lens (L2), identical to L1. To remove the pump photons, we use a second-half wave plate (HWP2) followed by a Glan-Thompson polarizer (GTP), such that the pump power is reduced by a factor equal to the extinction ratio of $\sim 10^5$. The resulting SFWM photon pairs are frequency non-degenerate and are split using a dichroic mirror (DM) followed by bandpass filters (BP1 and BP2) for further pump suppression. So as to characterise the behaviour of the photon pairs, both arms are coupled into multimode fibres (MMF1 and MMF2) using aspheric lenses with 8 mm focal length (L3 and L4). Each arm may be detected directly, with the multimode fibre in question (MMF1 or MMF2) leading to the input port of a silicon avalanche photodiode (APD1), or may be detected with spectral resolution using a monochromator that has been fitted with a multimode fibre (MMF3) ouptut, leading to a second silicon avalanche photodiode (APD2). In our setup we detect the signal (idler) arm directly and the idler (signal) arm with spectral resolution. The output signals from the two APDs are sent to a to a nuclear instrumentation module (NIM) coincidence circuit, based on discriminators and and a logic module, followed by an electronic pulse counter. In this manner, we obtain experimentally the coincidence spectra, corresponding to equation (16). Note that we may reverse the roles of the direct-detection and spectrally resolved arms so to obtain the coincidence spectra for both the signal and idler photons.

Our first technique for two-photon state spectral tuning of SFWM photon pairs involves the use of tapered fibres fabricated in our laboratory, with a varying waist radius. In the next subsection, we describe briefly the taper fabrication process and in section 3.3 we describe SFWM photon-pair generation with our taper devices.

3.2. Fabrication and characterisation of tapered fibres

Our tapered-fibre fabrication process is based on the flame-brushing technique, i.e stretching the bow-tie fibre under the application of heat through a flame [23, 24]. The ends of the optical fibre are fixed onto mounts which include high-precision fibre rotators (Thorlabs HRF007) for making sure that the fibre is torsion-free prior to stretching. An oxygen/butane flame is placed underneath the fibre, with the burner mounted on a linear motor which moves the flame back and forth along the fibre creating a section of the fibre which is heated nearly homogeneously. Meanwhile, the two fibre ends can be displaced laterally in opposite directions with the help of linear motors, which produces the fibre stretching. This results in a tapered fibre with a reduced radius in the waist and the appearance of two transition sections, preceding and following the waist.

In our tapering apparatus, we use oxygen/butane in a 2.6 proportion and displace the flame at a speed of 3 mm/s, while the stretching motors are displaced at a speed of 6 mm/minute. We have fabricated six different fibre tapers, all with waist length $L_w = 25$ mm, and with waist diameter given by fractions $s = 0.95, 0.90, 0.85, 0.80, 0.75,$ and, 0.70 of the unstretched cladding radius $D_0 = 80$ μm. Note that because the entire fibre cross-section is scaled down by factor s, the core radius is likewise reduced in the same proportion to $r_w = s r_0$. All tapers involve adiabatic transitions [25, 26], with the fibre radius versus z profile described by an exponential function in the two transition sections. In table 1 we summarise the physical parameters of our six fibre tapers along with a seventh unstretched fibre, each to be used for SFWM photon-pair generation.

While for the initial verification of the correct operation of our tapering apparatus we employed a scanning electron microscope to measure the diameter of our taper devices at different longitudinal locations, we also developed an alternative, *in situ*, and non-destructive test based on optical microscopy. For this test, we employ an optical microscope based on a 40× objective and CCD camera that can be scanned laterally along the fibre (with a maximum range of 30 cm), with the help of a linear motor. Image processing software automatically extracts an estimate of the fibre diameter at a given longitudinal location, with an approximate accuracy of ± 1 μm. The profile can then be compared with the one obtained from the volume-conservation model based on

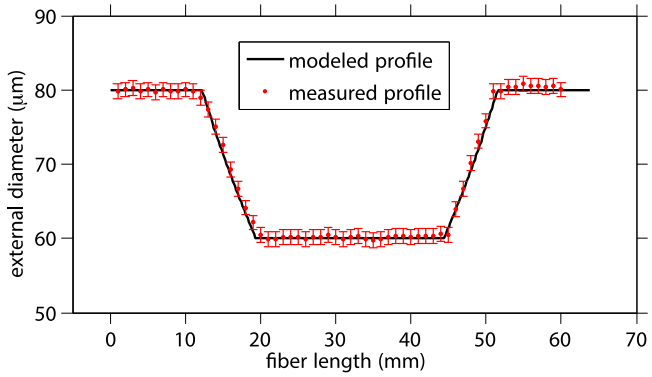

Figure 3. Taper profile with $L_w = 25$ mm and $r_w = 0.75r_0$. Red dots represent the measured profile, while the black line is the modelled profile [20].

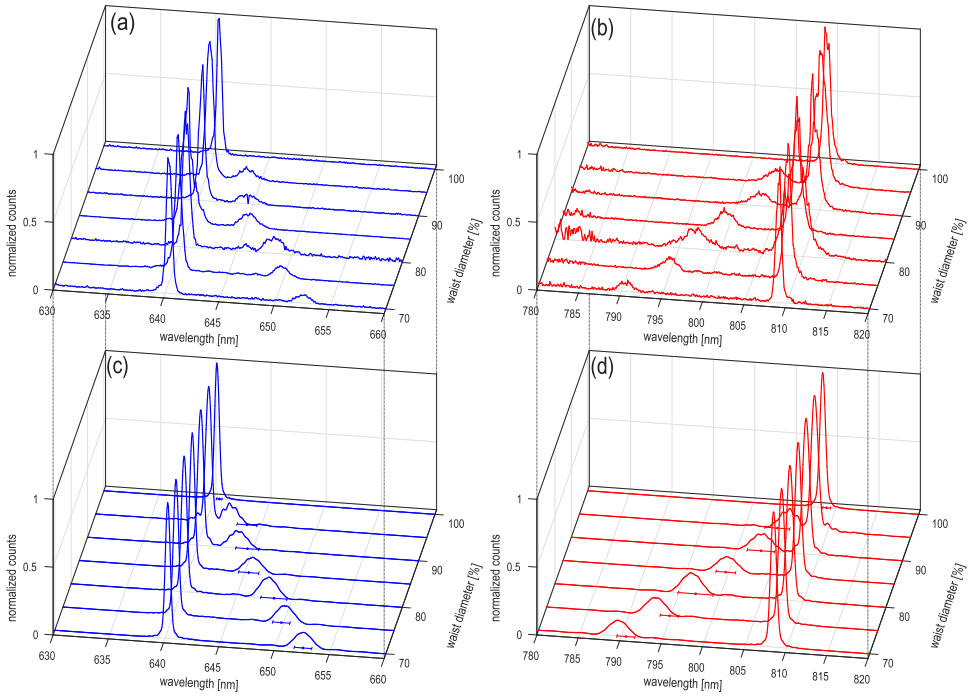

Figure 4. Emitted SFWM coincidence spectra as function of parameter s (expressed as a percentage). (a) Measured idler spectra. (b) Measured signal spectra. (c) Calculated idler spectra. (d) Calculated signal spectra. Note that in panels (c) and (d) the error bars, on the plane defined by wavelength and waist diameter axes, indicate the location of the peak and the measured bandwidth.

the work of Birks et al [20]. In figure 3 we show an example of such a measurement, for $s = 0.75$ (i.e. $r_w = 0.75r_0$), shown overlapped with a curve depicting the expected profile based on the model; note that our measurement agrees well with the model.

3.3. Measured SFWM spectra for tapered fibres

We use for our measurements the taper devices mentioned in the previous subsection, with core radii in the waist $r_w = sr_0$ ranging from $s = 1.0$ to 0.7, with $r_0 = 1.45$ μm; note that these tapers were fabricated using HB800C bow-tie fibre from Fibercore Ltd. We measure for each of these devices the coincidence spectrum of signal and idler photons, as described in section 3.1, as a function of the parameter s. The results for the idler and signal modes, respectively, are shown in figures 4(a) and (b). In panels (c) and (d), we show corresponding simulated spectra derived from the theory presented in section 2, to be discussed more fully in section 4.

Note that while for the unstretched fibre we observe a single peak for each of the signal and idler modes, for $s < 1$ this single peak splits into two peaks with the spectral separation between them increasing as s is reduced. One of these peaks remains fixed with the same centre frequency and shape as observed for the unstretched fibre, while the secondary peak is displaced in response to stretching. As discussed in section 4, the peak which remains

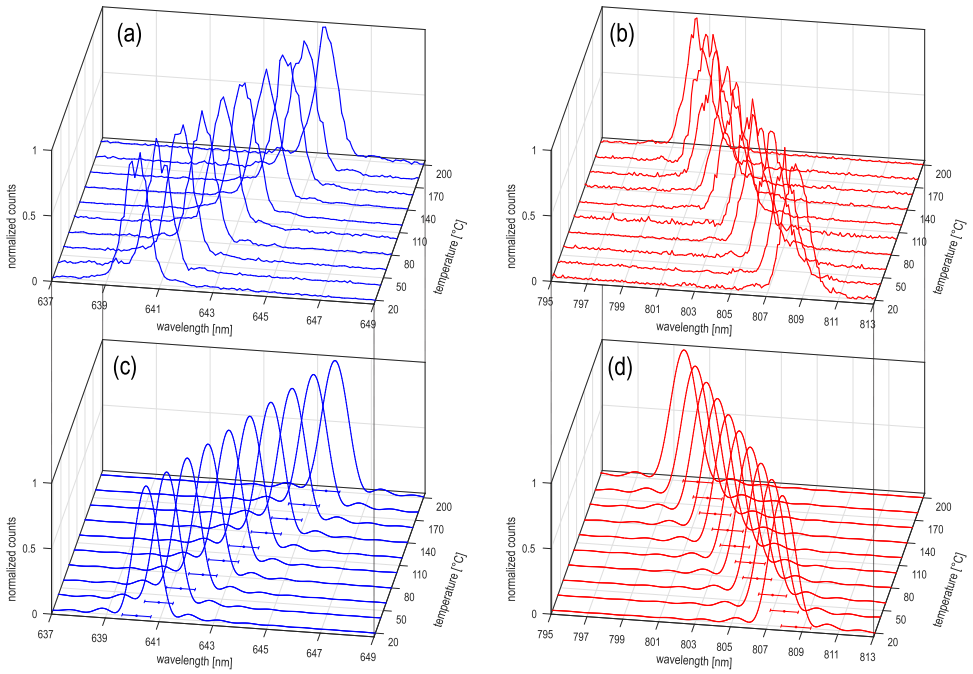

Figure 5. Emitted SFWM coincidence spectra as function of fibre temperature. (a) Measured idler spectra. (b) Measured signal spectra. (c) Calculated idler spectra. (d) Calculated signal spectra. Note that in panels (c) and (d) the error bars, on the plane defined by wavelength and temperature axes, indicate the peak maximum an experimental bandwidth.

stationary is associated with the unstretched portions of the fibre while the secondary peak is associated with the taper waist and its centre frequency can be controlled through the degree of stretching, quantified by s. The maximum spectral shift, in the secondary peak, observed for the signal (idler) photon is ∼18 nm (∼12 nm). Also note that stretching results in a shift of the signal and idler secondary peaks towards the pump wavelength, so that the signal-idler spectral separation decreases with decreasing s.

Note that two factors limit the maximum attainable degree of stretching. On the one hand, in the fibre stretching process as one decreases the value of s, at some point the core and cladding fuse into a single type of glass with the result that the air surrounding the fibre becomes the effective cladding [27]; one would expect a drastic change in the SFWM phasematching properties at this point. On the other hand, we point out that the bow-tie structure involving the core surrounded by two stress applying parts, or bows, is rather vulnerable to the stretching process [28, 29]. In the absence of torsion, the core and bows define a plane; any torsion will mean that when stretching the fibre, the bow-tie structure will be degraded or even altogether suppressed. While we have taken care to eliminate torsion in the fibre before the stretching process begins we observe that, due to an as yet unclear experimental imperfection for values of the waist radius involving $s < 0.7$, the outcoupled pump becomes depolarised so that rotation of HWP2 no longer permits the suppression of the pump, with the result that the measured SFWM spectra become rather noisy. For this reason we have kept fibre stretching within the regime $0.7 \leqslant s \leqslant 1$.

3.4. Measured SFWM spectra as a function of temperature

A second strategy for spectrally tuning the SFWM two-photon state involves using a fibre of the same specifications and same batch as used in our taper experiments, subjected to heating. A 4.5 cm length of fibre is housed within an oven which permits setting the temperature, with ± 0.05 °C accuracy, within a range covering from room temperature up to 200 °C. Note that the fibre length was chosen so that it fits fully within the oven.

Figures 5(a) and (b) show the coincidence spectra of the idler and signal arms, respectively, as a function of fibre temperature. In panels (c) and (d), we show corresponding simulated spectra derived from the theory presented in section 2, to be discussed more fully in section 4. The maximum spectral shift observed for the signal (idler) photon is ∼8.2 nm (∼5.1 nm); this corresponds to a spectral shift per unit temperature of 4.1×10^{-2} nm/°C (2.5×10^{-2} nm/°C), respectively. Also note that heating results in a shift of the signal and idler peaks towards the pump wavelength, so that the signal-idler spectral separation decreases with increasing temperature.

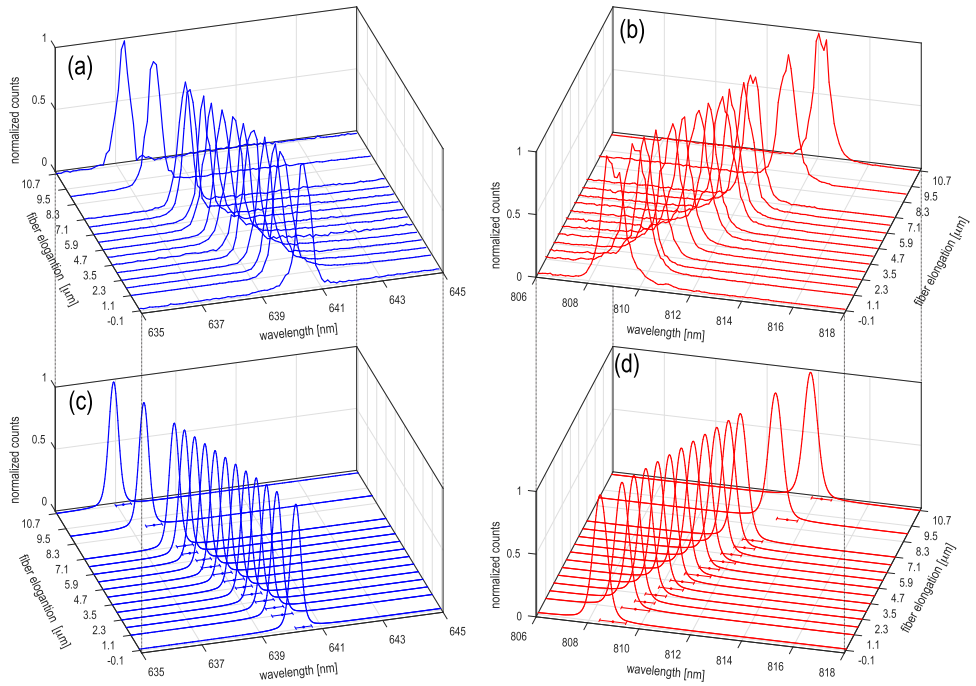

Figure 6. Emitted SFWM coincidence spectra as function of the fibre longitudinal stress, expressed in terms of the fibre elongation. (a) Measured idler spectra. (b) Measured signal spectra. (c) Calculated idler spectra. (d) Calculated signal spectra. Note that in panels (c) and (d) the error bars, on the plane defined by wavelength and fibre elongation axes, indicate the peak maximum and experimental bandwidth.

3.5. Measured SFWM spectra as a function of applied longitudinal stress

A third strategy for spectrally tuning the SFWM two-photon state involves the use of an (unstretched) fibre held at room temperature of the same specifications and same batch as used in our taper and temperature experiments subjected to the application of longitudinal stress. The fibre is glued at its two ends to mechanical mounts, one of which can be translated with a micrometre-fitted translation stage. We used a fibre of length 17.2 cm and have applied a maximum elongation of 10.7 μm, which corresponds to 0.06% of the original length.

Figures 6(a) and (b) show the coincidence spectra of the idler and signal arms, respectively, as a function of the longitudinal elongation of the fibre due to the applied longitudinal stress. In panels (c) and (d), we show corresponding simulated spectra derived from the theory presented in section 2, to be discussed more fully in section 4. The maximum spectral shift observed for the signal (idler) photon is ~5.3 nm (~3.2 nm); this corresponds to a spectral shift per unit elongation of 0.49 nm/μm (0.30 nm/μm), respectively. Also note that the application of longitudinal stress results in a shift of the signal and idler peaks away from the pump wavelength, so that the signal-idler spectral separation increases with increasing applied longitudinal stress.

4. Discussion

In this section we describe the analysis of the results obtained from the three techniques implemented for spectrally tuning the SFWM two-photon state. Based on our theory of the SFWM process in optical fibres (see section 2 and reference [22]), we are able to explain the origin of the spectral shifting in all three cases.

4.1. Spectral tunability by fibre-tapering technique

In an optical fibre, the effective dispersion has a material contribution as well as a waveguide contribution [19]. While the material contribution is not affected by tapering, the waveguide contribution is strongly radius-dependent and as such can be controlled by tapering. This implies that the SFWM phasematching properties, governed by dispersion, will likewise be strongly affected by tapering; each core radius r in a fibre's radius profile can lead to characteristic phasematched frequencies $\omega_s(r)$ and $\omega_i(r) = 2\omega_p - \omega_s(r)$ for the signal and idler, respectively.

In a fibre taper such as the one sketched in figure 1, there is in fact a continuum of core radii ranging from r_0 (in the unstrecthed regions) to r_w (at the waist). This implies a continuum of phasematched frequencies: for example in the signal arm covering from $\omega_s(r_0)$ through $\omega_s(r_w)$. However, the conversion efficiency is not

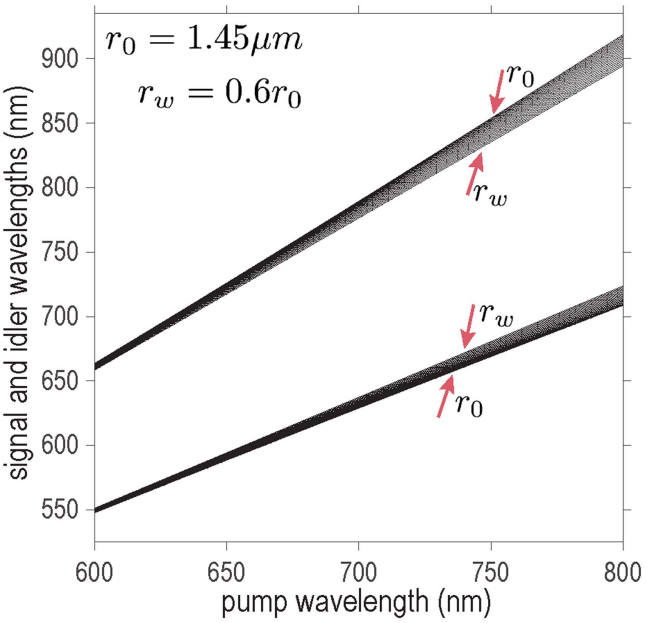

Figure 7. Phasematching diagram for a fibre taper for which the numerical aperture and birefringence remain constant along the taper length.

constant across this entire bandwidth. As can be seen in figure 4 (panels (a) and (b)), for all of the tapers described in table 1 the measured spectra exhibit two characteristic spectral peaks, which are centred at $\omega_s(r_0)$ and $\omega_s(r_w)$ for the signal, and at $\omega_i(r_0)$ and $\omega_i(r_w)$ for the idler. Note that since $\omega_s(r_0)$ and $\omega_i(r_0)$ are associated with the unstretched portions, they remain fixed as the parameter s is decreased. In contrast, $\omega_s(r_w)$ and $\omega_i(r_w)$ shift appreciably, as expected, as s is decreased. Focusing on the spectral peaks centred at $\omega_s(r_w)$ and $\omega_i(r_w)$, our results thus suggest that fibre tapering can be employed as a spectral tuning technique for SFWM photon pairs.

For a given taper, the generation rate at specific spectral components $\omega_s(r)$ and $\omega_i(r)$, will be governed by the fraction of the total taper length over which the radius r is maintained. In our tapers, radius r_0 is maintained over a region of length $2L_c$ and radius r_w is maintained over a region of length L_w. Because for all six of our taper devices $2L_c > L_w$, the peaks at $\omega_s(r_0)$ and $\omega_i(r_0)$ are higher than those at $\omega_s(r_w)$ and $\omega_i(r_w)$. Note that the maximum attainable ratio $L_w/(2L_c)$ is limited by the dimensions of the two high-precision fibre rotators with a combined length of 14 cm, used to maintain the fibres in place during both the tapering process and the SFWM experiments. A future refinement could entail cutting off most of the unstretched portions and holding the fibre through some other means, with the result of enhancing the relative heights of the pair of peaks which respond to tapering. All intermediate radii between r_0 and r_w are only maintained each over a small fraction of $2z_0$ (the combined length of the two transitions), implying that there is no appreciable generation rate at the intermediate frequencies. Note, however, that a taper with very long transitions could result in a 'plateau' appearing in the SFWM spectra, between $\omega_s(r_0)$ and $\omega_s(r_w)$ for the signal and $\omega_i(r_0)$ and $\omega_i(r_w)$ for the idler. This could potentially serve as a strategy for generating broadband photon pairs. This discussion is illustrated in figure 7, which shows phasematched signal and idler wavelengths plotted as a function of the pump wavelength, for a bow-tie fibre taper characterised by $s = 0.6$. Each branch, corresponding to signal and ilder, of this phasematching diagram has a thickness, with the outer extreme corresponding to our estimate for $\omega_\mu(r_0)$ and the inner extreme corresponding to our estimate for $\omega_\mu(r_w)$ (with $\mu = s,\ i$).

Note from figures 4(a) and (b) that the secondary peaks in the idler arm (with $\lambda < \lambda_p$) shifts up to 12 nm and the corresponding ones in the signal arm (with $\lambda > \lambda_p$) shifts up to 18 nm when r_w varies from 1.45 μm to 1.015 μm (i.e. corresponding to decreasing s from $s = 1$ to $s = 0.7$). It turns out that these spectral shifts are larger than would be expected from an analysis based solely on the effect of the reduced core radius on the fibre dispersion, as in figure 7. To explain this discrepancy, let us recall that in our experiments we use bow-tie fibres in which the bows introduce a mechanical stress field within the fibre which leads to birefringence. It is entirely feasible that during the taper fabrication process this stress field will be affected leading to a modified (increased or decreased) birefringence, leading in turn to modified SFWM phasematching properties. Our approach was then to tweak in our simulations the fibre birefringence Δ at the taper waist, for each value of s, until the theory spectra would best match the experimental spectra. Figure 8(a) shows (magenta square markers) the birefringence values obtained through this optimisation procedure for our tapers along with the reference fibre ($s = 1$), as a function of s. The data shows clearly that as the waist radius is decreased, the fibre birefringence Δ

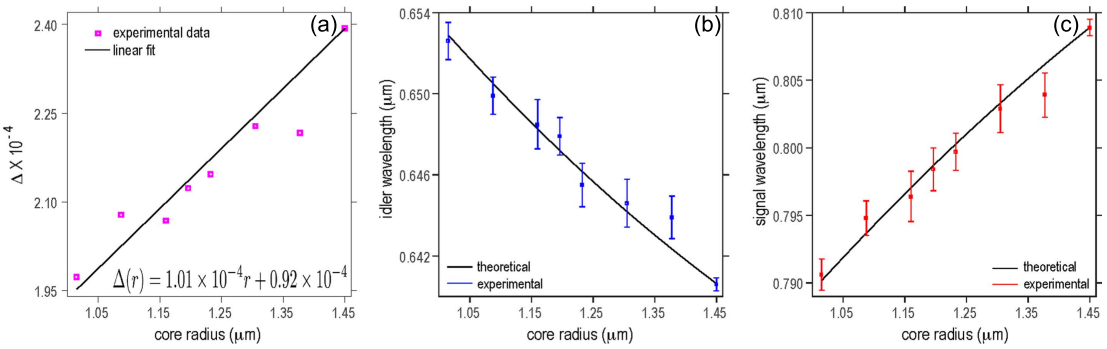

Figure 8. (a) Fibre birefringence (Δ) as function of core radius. (b) Dependence of the emitted idler wavelengths on the core radius. (c) Dependence of the emitted signal wavelengths on the core radius. Error bars indicate the experimental generation bandwidth.

also decreases. Fitting the data to a linear relationship, with the constraint that it yields the known Δ value for the reference fibre, it was found that for our bow-tie fibre, Δ varies with the core radius according to the relationship $\Delta(r) = 1.01 \times 10^{-4} r + 0.92 \times 10^{-4}$ (with r expressed in μm); we have plotted this relationship as solid black line in figure 8(a).

It is interesting to note that tapering leads to a *reduction* of the birefringence in our bow-tie fibre, suggesting that stretching under the application of heat results in a relaxation of the initial mechanical stress field in the fibre.

Armed with a full understanding of how tapering leads to a modified dispersion due to (i) the effect of a reduced core radius and (ii) to a modified birefringence, we have computed the SFWM coincidence spectra derived from our model, and have shown them in figures 4(c) and (d). Note that there is an excellent agreement, both in terms of the relative heights of the peaks and their central frequencies, between theoretical and experimentally-measured spectra. In addition, we have plotted in figures 8(b) and (c) (black solid line) the expected central peak frequencies $\omega_s(r_w)$ and $\omega_i(r_w)$ for the signal and idler, as a function of parameter s, along with the values obtained from the measured spectra, see figures 4, panels (a) and (b) (with blue markers for the idler and red markers for the signal). For each of these markers, we have indicated with an error bar the $1/e$ width of the corresponding peaks. Again, note the excellent agreement between the experimental measurements and the expected behaviour derived from the model.

4.2. Spectral tunability by temperature variation technique

As we have shown in section 3.4, heating our SFWM bow-tie fibre results in spectral shifting of the photon-pair spectra. Let us first point out that the refractive index of fused silica has a temperature dependence so that the dispersion experienced by the four participating waves in the SFWM process likewise has a temperature dependence [30]. However, we have verified that for fused silica the effect of temperature-induced variations in the index of refraction on the phasematching properties is essentially negligible, with <0.8 nm shifting of the SFWM peaks when heating from 20 °C to 200 °C. Also, when heating the fibre the core radius will increase due to thermal expansion. However, fused silica has a low thermal expansion coefficient (0.5×10^{-6}/°C) [31], so that heating from 20 °C to 200 °C leads to an increase in the core radius of $<1.5 \times 10^{-4}$ μm, which in turn leads to a negligible shift in the SFWM peaks.

Following an analysis similar to the case of fibre tapering, we identify that the spectral tuning of the SFWM signals is due to variations in the birefringence of the bow-tie fibre when it is subjected to heating. Our approach is as follows: we tweak the fibre birefringence Δ in our simulations, for each value of the temperature, until the theory spectra best match the experimental spectra. Figure 9(a) shows (magenta square markers) the birefringence values obtained through this optimisation procedure as a function of temperature. The data shows clearly that as the temperature is increased, the fibre birefringence Δ decreases [32]. Fitting the data to a linear relationship, it was found that the birefringence for the bow-tie fibre used in the experiment varies with temperature according to the relation: $\Delta(T) = -1.8 \times 10^{-7}\, T + 2.4 \times 10^{-4}$ (with the temperature T expressed in °C); the black solid line in the figure represents this linear relationship.

It is interesting to note that heating the fibre leads to a *reduction* of the birefringence in our bow-tie fibre [32], suggesting that in this respect heating leads to a similar effect than fibre tapering and results in a relaxation of the initial mechanical stress field in the fibre [33, 34].

Taking into account the dependence of the birefringence on temperature which we have determined, we calculate the signal and idler wavelengths for which perfect phasematching is achieved in the temperature range $T = 20$ °C–200 °C. The results are shown in figures 9(c) and (b), respectively, by the black solid line. In these

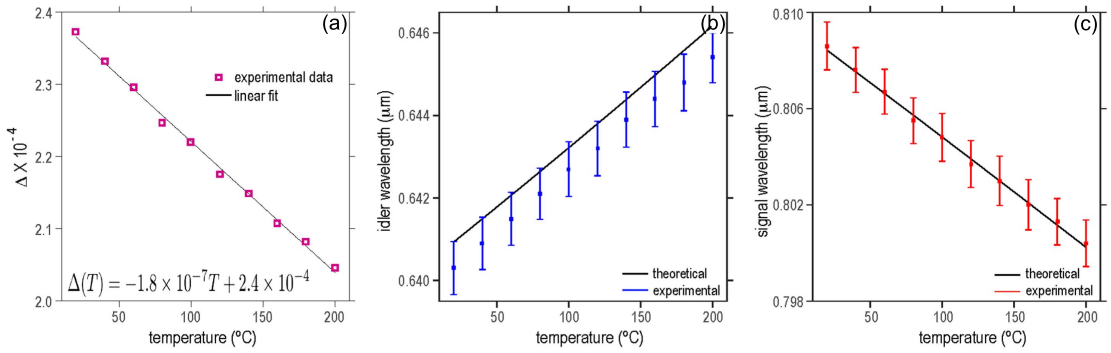

Figure 9. (a) Fibre birefringence (Δ) as function of temperature. (b) Dependence of the emitted idler wavelengths on temperature. (c) Dependence of the emitted signal wavelengths on temperature. Error bars indicate the experimental generation bandwidth.

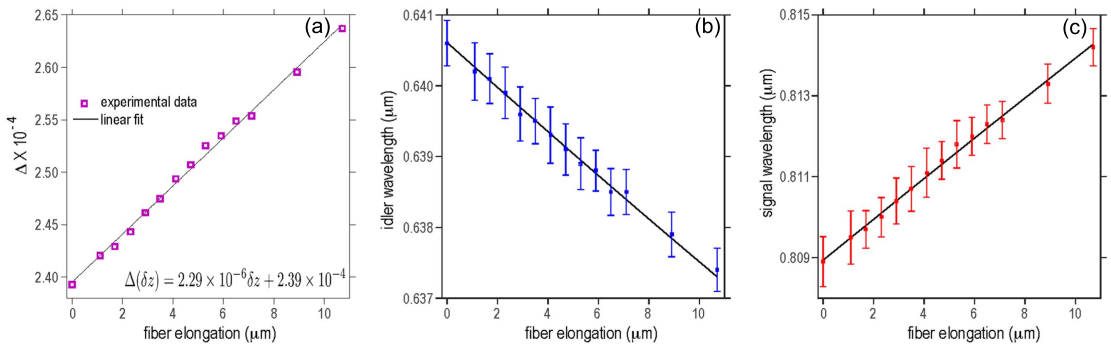

Figure 10. (a) Fibre birefringence (Δ) as function of the tensile strength, expressed in terms of fibre elongation. (b) Dependence of the emitted idler wavelengths on fibre elongation. (c) Dependence of the emitted signal wavelengths on fibre elongation. Error bars indicate the experimental generation bandwidth.

same figures square markers (blue for idler and red for signal) are the values obtained from the maxima of the measured spectra (see figures 5, panels (a) and (b)) and the error bars indicate the generation bandwidth, i.e. the $1/e$ peak width. We note that there is a slight discrepancy in the case of the idler of <1 nm which we attribute to a slight monochromator miscalibration; note that in our optimisation routine used for the determination of the the birefringence we have used the signal frequencies and have obtained the idler counterparts through energy conservation.

4.3. Spectral tunability through the application of longitudinal stress

For the case of a birefringent fibre with constant core radius along its length and kept at room temperature, tunability of the emitted spectra can be achieved by applying longitudinal tension to the fibre [35, 36] as can be seen from the measured coincidence spectra shown in figures 6(a) and (b). Note that the reduction of the core radius resulting from the elongation applied (10.7 μm with an initial length of 17.2 cm) is of the order of 4.5×10^{-5} μm which results in a negligible shift in the SFWM peaks. Note also from figure 6 that under the conditions of our experiment, a maximum displacement of 5.3 nm was obtained in the signal arm ($\lambda > \lambda_p$) and 3.2 nm in the idler arm ($\lambda < \lambda_p$). Following an analysis similar to the cases of fibre tapering and temperature variations, we identify that the spectral tuning of the SFWM photon pairs is due to variations in the birefringence of the bow-tie fibre under the application of longitudinal stress. Our approach is similar to that used for the cases of fibre tapering and temperature variations: we tweak the fibre birefringence Δ in our simulations, for each degree of longitudinal stretching, until the theory spectra best match the experimental spectra. Figure 10(a) shows (magenta square markers) the birefringence values obtained through this optimisation procedure as a function of the degree of longitudinal elongation. The data shows clearly that as the fibre is subjected to an increased longitudinal stress, the fibre birefringence Δ increases. Fitting the data to a linear relationship, it was found that the birefringence for the bow-tie fibre used in the experiment varies with the degree of longitudinal elongation according to the relation: $\Delta(\delta z) = 2.29 \times 10^{-6}\, \delta z + 2.39 \times 10^{-4}$ (with δz expressed in μm); the black solid line in the figure represents this linear relationship.

It is interesting to note that applying longitudinal stress leads to an *increase* of the birefringence in our bow-tie fibre, in direct contrast to the behaviour observed for fibre tapering and heating. It seems reasonable that

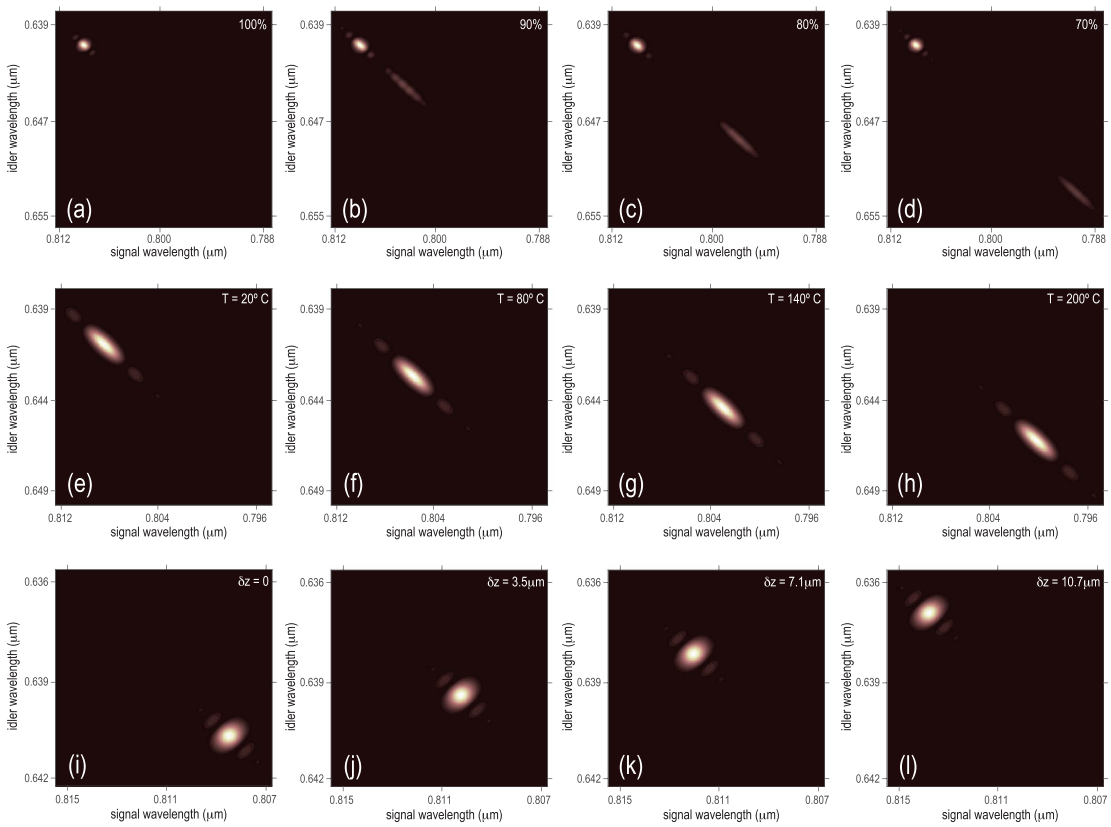

Figure 11. Theoretical joint spectral intensity, calculated assuming the physical parameters of our implemented SFWM source. (a)–(d) Results of fibre tapering. (e)–(h) Results of fibre heating. (i)–(l) Results of longitudinal stress.

application of longitudinal tension, tends to sharpen the initial mechanical stress field in the fibre [37, 38]. It is because of this behaviour, which contrasts with that observed for tapering and heating, that the signal-idler spectral separation increases through this SFWM tuning mechanism, while it decreases for the other two mechanisms.

Taking into account the dependence of the birefringence on the application of longitudinal stress which we have determined, we calculate the signal and idler wavelengths for which perfect phasematching is achieved under the application of longitudinal stress resulting in an elongation of up to 10.7 μm. The results are shown in figures 10(c) and (b), respectively, by the black solid line. In these same figures square markers (blue for idler and red for signal) are the values obtained from the maxima of the measured spectra (see figure 6, panels (a) and (b)) and the error bars indicate the generation bandwidth, i.e. the $1/e$ peak width.

4.4. Behaviour of joint spectral intensity under spectral shifting

While in our experiments we measured the coincidence spectra (involving a spectrally resolved signal mode) rather than the full joint spectrum $|G(\omega_s, \omega_i)|^2$, it is interesting to plot the expected joint spectrum from our theory and observe how it behaves under the three spectral tuning mechanisms which we have discussed here. In figure 11 we show the results of such an exercise where the first row corresponds to fibre tapering, the second row corresponds to heating and the third row corresponds to the application of longitudinal stress. We plotted four joint spectra for decreasing values of s from left to right (first row), increasing temperature (second row) and increasing applied longitudinal stress (third row). It is interesting to note that while the spectral tuning is evident in all three cases, the shape of the joint spectrum, and therefore the type of spectral correlations, remain essentially unaffected by the spectral tuning, again in all three cases.

5. Conclusions

In this paper we explored three different mechanisms for achieving spectral tunability of photon pairs generated through the spontaneous four-wave mixing process. The first of these mechanisms is the use of fibre tapering, which exploits the dependence of the optical dispersion experienced by the four waves on the core radius. We presented a theory of SFWM for tapered fibres and experimental measurements of the emitted coincidence

spectra for a collection of tapers in which the core radius at the taper waist ranges from 70% to 100% of the original, untapered core radius. We found that the core radius-dependent dispersion is not sufficient to explain the observed spectral tuning; it turns out that when fabricating a taper the birefringence of the fibre is also affected and must be taken into account.

We explored two other mechanisms for attaining photon-pair spectral tuning: temperature variation and application of longitudinal stress. Although the maximum spectral shift observed with these two techniques is smaller than for the tapering technique, these two mechanisms are considerably simpler to implement and have the important advantage that they are based on the use of a single, suitably controlled fibre specimen. We note that another possibility which could be explored for SFWM photon-pair spectral tuning is the use of transverse (compressive) stress which has been shown to result in variation of the fibre birefringence [39]. We hope that these results will enable future progress in practical applications of fibre-based photon-pair sources.

Acknowledgements

This work was supported by CONACYT (grants 222928, 253366, 271322 and 221052), by PAPIIT(UNAM) grant IN1050915, and by AFOSR grant FA9550-16-1-0458.

References

[1] Giovannetti V, Lloyd S and Maccone L 2011 Advances in quantum metrology *Nat. Photon.* **5** 222–9
[2] Gissin N and Thew R 2007 Quantum communication *Nat. Photon.* **1** 165–71
[3] Kok P, Munro W J, Nemoto K, Ralph T C, Dowling J P and Milburn G J 2007 Linear optical quantum computing with photonic qubits *Rev. Mod. Phys.* **79** 797
[4] Fiorentino M, Voss P L, Sharping J E and Kumar P 2002 All-fiber photon-pair source for quantum communications *IEEE Photon. Technol. Lett.* **14** 983–5
[5] Sharping J E, Lee K F, Foster M A, Turner A C, Schmidt B S, Lipson M, Gaeta A L and Kumar P 2006 Generation of correlated photons in nanoscale silicon waveguides *Opt. Express* **14** 12388–93
[6] Smith B J, Mahou P, Cohen O, Lundeen J S and Walmsley I A 2009 Photon pair generation in birefringent optical fibers *Opt. Express* **17** 23589–602
[7] Fang B, Cohen O and Lorenz V O 2014 Polarization-entangled photon-pair generation in commercial-grade polarization-maintaining fiber *J. Opt. Soc. Am.* B **31** 277–81
[8] Garay-Palmett K, McGuinness H J, Cohen O, Lundeen J S, Rangel-Rojo R, U'Ren A B, Raymer M G, McKinstrie C J, Radic S and Walmsley I A 2007 Photon pair-state preparation with tailored spectral properties by spontaneous four-wave mixing in photonic-crystal fiber *Opt. Express* **15** 14870
[9] McGuinness H J, Raymer M G, McKinstrie C J and Radic S 2010 Quantum frequency translation of single-photon states in a photonic crystal fiber *Phys. Rev. Lett.* **105** 093604
[10] Chen D, Sun B and Wei Y 2010 Multi-wavelength laser source based on enhanced four-wave-mixing effect in a highly nonlinear fiber *Laser Phys.* **20** 1733
[11] Pang F, Xiang W, Guo H, Chen N, Zeng X, Chen Z and Wang T 2008 Special optical fiber for temperature sensing based on cladding-mode resonance *Opt. Express* **16** 12967
[12] Monro T M, West Y D, Hewak D, Wm Broderick N G R and Richardson D J 2000 Chalcogenide holey fibres *Electron. Lett.* **36** 1998–2000
[13] Vanvincq O, Travers J C and Kudlinski A 2011 Conservation of the photon number in the generalized nonlinear Schrodinger equation in axially varying optical fibers *Phys. Rev.* A **84** 063820
[14] Coillet A, Vienne G and Grelu P 2010 Potentialities of glass air-clad micro and nanofibers for nonlinear optics *J. Opt. Soc. Am.* B **27** 394–401
[15] Birks T A, Wadsworth W J and Russell P 2000 Supercontinuum generation in tapered fibers *Opt. Lett.* **25** 1415–7
[16] Lee T, Jung Y, Codemard C A, Ding M, Broderick N G and Brambilla G 2012 Broadband third harmonic generation in tapered silica fibres *Opt. Express* **20** 8503–11
[17] Cui L, Li X, Guo C, Li Y H, Xu Z Y, Wang L J and Fang W 2013 Generation of correlated photon pairs in micro/nano-fibers *Opt. Lett.* **38** 5063–6
[18] Garay-Palmett K, U'Ren A B and Rangel-Rojo R 2010 Conversion efficiency in the process of copolarized spontaneous four-wave mixing *Phys. Rev.* A **82** 043809
[19] Agrawal G P 2001 *Nonlinear Fibre Optics* 3rd edition (Cambridge, MA: Academic Press) pp 389–444
[20] Birks T A and Li Y W 1992 The shape of fiber tapers *J. of Lightwave Technology* **10** 432–8
[21] Cruz-Delgado D, Ramirez-Alarcon R, Ortiz-Ricardo E, Monroy-Ruz J, Dominguez-Serna F, Cruz-Ramirez H, Garay-Palmett K and U'Ren A B 2016 Fiber-based photon-pair source capable of hybrid entanglement in frequency and transverse mode, controllably scalable to higher dimensions *Sci. Rep* **6** 277377
[22] Garay-Palmett K, Cruz-Delgado D, Dominguez-Serna F, Ortiz-Ricardo E, Monroy-Ruz J, Cruz-Ramirez H, Ramirez-Alarcon R and U'Ren A B 2016 Photon pair generation by intermodal spontaneous four wave mixing in birefringent weakly guiding optical fibers *Phys. Rev.* A **93** 033810
[23] Brambilla G 2010 Optical fibre nanowires and microwires: a review *J. Opt.* **12** 043001
[24] Jung Y, Brambilla G and Richardson D J 2010 Polarization-maintaining optical microfiber *Opt. Lett.* **35** 2034–6
[25] Love J D, Henry W M, Stewart W J, Black R J, Lacroix S and Gonthier F 1991 Tapered single-mode fibres and devices :I. Adiabaticity criteria *IEE ProceedingsJ* **138** 343–54
[26] Black R J, Lacroix S, Gonthier F and Love J D 1991 Tapered single-mode fibres and devices : II. Experimental and theoretical quantification *IEE ProceedingsJ* **138** 355–64

[27] Hoffman J E, Fatemi F K, Beadie G, Rolston S L and Orozco L A 2015 Rayleigh scattering in an optical nanofiber as a probe of higher-order mode propagation *Optica* **2** 416–23
[28] Biancalana F, Skryabin D V, Russell P St and Four-wave J 2003 mixing instabilities in photonic-crystal and tapered fibers *Phys. Rev.* E **68** 046603
[29] Noda J, Okamoto K and Sasaki Y 1986 Polarization-maintaining fibers and their applications *J. of Lightwave Technology* **8** 1071–89
[30] Ghosh G, Endo M and Iwasaki T 1994 Temperature-dependent Sellmeier coefficients and chromatic dispersions for some optical fiber glasses *J. of Lightwave* T **12** 1338–42
[31] Roy R, Agrawal D K and McKinstry H A 1989 Very low thermal expansion coefficient materials *Annu. Rev. Mater. Sci.* **19** 59–81
[32] Michie A, Canning J, Lyytikainen K, Aslund M and Digweed J 2004 Temperature independent highly birefringent photonic crystal fibre *Opt. Express* **12** 516–5
[33] Fontaine M, Wu B, Tzolov B P, Bock W J and Urbanczyk W 1996 Theoretical and experimental analysis of thermal stress effects on modal polarization properties of highly birefringent optical fibers *J. of Lightwave Technology* **14** 585–91
[34] Liu Y, Rahman B A and Grattan K T V 1994 Thermal-stress-induced birefringence in bow-tie optical fibers *Opt. Express* **33** 5611–6
[35] Jo Lee K, Hwang I, Chul P H and Yoon Kim B 2009 Axial strain dependence of all-fiber acousto-optic tunable filters *Opt. Express* **17** 2348–57
[36] Jeakwon K, Kwang J L and Byoung Y K 2014 Spectral shaping of an all-fiber torsional acousto-optic tunable filter *Appl. Opt* **53** 8499–506
[37] Schreiber T, Schultz H, Schmidt O, Roser F, Limpert J and Tannermann A 2005 Stress-induced birefringence in large-mode-area micro-structured optical fibers *Opt. Express* **13** 3637–46
[38] Christopher R D and Peter M W 2010 Sensitivity of Bragg gratings in birefringent optical fiber to transverse compression between conforming materials *Appl. Opt.* **49** 2250–61
[39] Silva-Lopez M, Li C, MacPherson N, Moore A J, Barton J S, Jones J D C, Zhao D, Zhang L and Bennion I 2004 Differential birefringence in Bragg gratings in multicore fiber under transverse stress *Opt.Lett.* **29** 2225–7